The Astrophysical Journal Letters, 955:L17 (14pp), 2023 September 20 https://doi.org/10.3847/2041-8213/acf0c5

Small Region, Big Impact: Highly Anisotropic Lyman-continuum Escape from a Compact Starburst Region with Extreme Physical Properties

Keunho J. Kim[1], Matthew B. Bayliss[1], Jane R. Rigby[2], Michael D. Gladders[3,4], John Chisholm[5], Keren Sharon[6], Håkon Dahle[7], T. Emil Rivera-Thorsen[8], Michael K. Florian[9], Gourav Khullar[10], Guillaume Mahler[11,12], Ramesh Mainali[2], Kate A. Napier[6], Alexander Navarre[1], M. Riley Owens[1], and Joshua Roberson[1]

[1] Department of Physics, University of Cincinnati, Cincinnati, OH 45221, USA; kim2k8@ucmail.uc.edu
[2] Observational Cosmology Lab, Code 665, NASA Goddard Space Flight Center, 8800 Greenbelt Road, Greenbelt, MD 20771, USA
[3] Department of Astronomy and Astrophysics, University of Chicago, 5640 South Ellis Avenue, Chicago, IL 60637, USA
[4] Kavli Institute for Cosmological Physics, University of Chicago, 5640 South Ellis Avenue, Chicago, IL 60637, USA
[5] Department of Astronomy, The University of Texas at Austin, 2515 Speedway, Stop C1400, Austin, TX 78712, USA
[6] Department of Astronomy, University of Michigan, 1085 South University Avenue, Ann Arbor, MI 48109, USA
[7] Institute of Theoretical Astrophysics, University of Oslo, P.O. Box 1029, Blindern, N-0315 Oslo, Norway
[8] The Oskar Klein Centre, Department of Astronomy, Stockholm University, AlbaNova, SE-10691 Stockholm, Sweden
[9] Steward Observatory, University of Arizona, 933 North Cherry Avenue, Tucson, AZ 85721, USA
[10] Department of Physics and Astronomy and PITT PACC, University of Pittsburgh, Pittsburgh, PA 15260, USA
[11] Institute for Computational Cosmology, Durham University, South Road, Durham DH1 3LE, UK
[12] Centre for Extragalactic Astronomy, Durham University, South Road, Durham DH1 3LE, UK

Received 2023 May 21; revised 2023 August 11; accepted 2023 August 15; published 2023 September 27

Abstract

Extreme, young stellar populations are considered to be the primary contributor to cosmic reionization. How the Lyman continuum (LyC) escapes these galaxies remains highly elusive, and it is challenging to observe this process in actual LyC emitters without resolving the relevant physical scales. We investigate the Sunburst Arc, a strongly lensed LyC emitter at $z = 2.37$ that reveals an exceptionally small-scale (tens of parsecs) region of high LyC escape. The small (<100 pc) LyC-leaking region has extreme properties: a very blue UV slope ($\beta = -2.9 \pm 0.1$), a high ionization state ([O III] $\lambda5007$/[O II] $\lambda3727 = 11 \pm 3$ and [O III] $\lambda5007/\mathrm{H}\beta = 6.8 \pm 0.4$), strong oxygen emission (EW([O III]) $= 1095 \pm 40$ Å), and a high Lyα escape fraction (0.3 ± 0.03), none of which are found in nonleaking regions of the galaxy. The leaking region's UV slope is consistent with approximately "pure" stellar light that is minimally contaminated by the surrounding nebular continuum emission or extinguished by dust. These results suggest a highly anisotropic LyC escape process such that LyC is produced and escapes from a small, extreme starburst region where the stellar feedback from an ionizing star cluster creates one or more "pencil-beam" channels in the surrounding gas through which LyC can directly escape. Such anisotropic escape processes imply that random sight-line effects drive the significant scatters between measurements of galaxy properties and LyC escape fraction, and that strong lensing is a critical tool for resolving the processes that regulate the ionizing budget of galaxies for reionization.

Unified Astronomy Thesaurus concepts: Lyman-alpha galaxies (978); Reionization (1383); Strong gravitational lensing (1643); Emission line galaxies (459); Starburst galaxies (1570); Galaxy structure (622)

1. Introduction

Cosmic reionization is the last major phase transition of the Universe, when most of the neutral hydrogen (H I) in the intergalactic medium (IGM) became ionized. Our current understanding of the luminosity functions and Lyman-continuum (LyC) escape fractions of active galactic nuclei and star-forming galaxies suggests that low-metallicity star-forming galaxies are likely the dominant contributors to the reionization process (Fan et al. 2006; Robertson et al. 2015; Finkelstein et al. 2019; Naidu et al. 2020; Yung et al. 2020).

However, the escape process of LyC radiation is complex, and only a small fraction of star-forming galaxies are confirmed LyC leakers. This strongly suggests that the escape process crucially depends on the geometry of the interstellar medium (ISM), dust screening effects, and the properties of the ionizing stars (Zackrisson et al. 2013; Verhamme et al. 2015; Chisholm et al. 2019).

What makes a galaxy a LyC emitter? Over a wide range of redshift ($0.02 < z < 4$), LyC emitters typically have young (<10 Myr) stellar populations, low metallicity ($12 + \log(\mathrm{O/H}) < 8.5$), extreme nebular emission line ratios (notably optical [O III] $\lambda5007$/[O II] $\lambda3727 > 5$), and little dust ($E(B - V) < 0.2$; Bergvall et al. 2006; Leitet et al. 2013; Borthakur et al. 2014; Mostardi et al. 2015; Izotov et al. 2016b, 2016a, 2018a, 2018b; Leitherer et al. 2016; Rutkowski et al. 2016, 2017; Shapley et al. 2016; Vanzella et al. 2018; Wang et al. 2019; Malkan & Malkan 2021; Chisholm et al. 2022; Flury et al. 2022a; Marques-Chaves et al. 2022). They also show a strong Lyα emission line in their UV spectra, which suggests a low column density of H I in the ISM and a favorable geometry for the escape of both Lyα and LyC photons (e.g., Verhamme et al. 2015; Rivera-Thorsen et al. 2017). In particular, there is recent evidence that LyC escape is highly anisotropic, with complex ISM geometries resulting in high LyC escape along a few narrow lines of sight with small solid angles (Rivera-Thorsen et al. 2019; Gazagnes et al. 2020;

Ramambason et al. 2020). Directly observing such "pencil-beam" channels of LyC requires extremely high angular resolution observations of known LyC-leaking galaxies.

Notably, LyC emitters show compact morphology with concentrated star formation, as indicated by a high star formation rate surface density ($\Sigma\mathrm{SFR} > 1\,M_\odot\,\mathrm{yr}^{-1}\,\mathrm{kpc}^{-2}$; Bergvall et al. 2006; Borthakur et al. 2014; Izotov et al. 2016b, 2016a, 2018b, 2018a; Wang et al. 2019; Ji et al. 2020; Kim et al. 2020, 2021; Flury et al. 2022a). Such a compact morphology of LyC emitters is closely related to the unresolved star cluster–like compact star-forming regions shown in their UV-continuum images.

Although these properties of LyC emitters show the overall galaxy properties, understanding the detailed LyC escape mechanisms—that is, where in a galaxy LyC radiation originates and how it escapes—crucially requires clear spatial information about the leaking galaxy to nail down the distribution of ionizing stars and the geometry of the surrounding nebular gas.

To date, such detailed morphologies (<100 pc scale) of LyC emitters have only been obtained for one LyC emitter (aka the Sunburst Arc) at $z = 2.37$ that is strongly lensed by a foreground galaxy cluster at $z = 0.44$ (Dahle et al. 2016). This is because the subgalactic-scale analysis is only possible in strongly lensed LyC-leaking galaxies like the Sunburst Arc due to lensing magnification. We cannot even spatially resolve the LyC-leaking regions of local ($z \sim 0$) LyC emitters because the only instrument with the ability to measure their ionizing photons is the Cosmic Origins Spectrograph (COS) on the Hubble Space Telescope (HST), which has a spectroscopic aperture diameter of 2."5. This means that LyC photons measured from COS cannot be localized on scales smaller than the COS aperture. As an example, for the local LyC-leaking galaxy Haro 11 (Bergvall et al. 2006; Leitet et al. 2011; Östlin et al. 2021) at a redshift of $z = 0.02$ (Bergvall & Olofsson 1986; Bergvall et al. 2006), the COS aperture corresponds to a region of ∼1 kpc in diameter (see Figure 1 of Östlin et al. 2021 for details).

Unlensed distant ($2.5 \lesssim z \lesssim 3.5$) LyC leakers are observable with HST WFC3/UVIS, but at these cosmological distances, even HST is limited to spatial scales of $\gtrsim$0.4 kpc. Strongly lensed LyC-leaking galaxies like the Sunburst Arc uniquely enable spatially resolved direct studies of LyC escape on the physical scales of individual star clusters.

Thus, the most detailed spatial information about LyC emitters may be obtained from the Sunburst Arc. Due to lensing magnification, the galaxy's stretched rest-frame LyC image reveals that only one particular star-forming region shows escaping ionizing radiation, while other regions within the galaxy do not (Rivera-Thorsen et al. 2019). Indeed, due to its uniqueness as a bright lensing-magnified LyC emitter, the Sunburst Arc has been of great interest in numerous studies concerning the physics of ionizing radiation production and escape (Rivera-Thorsen et al. 2017, 2019; Chisholm et al. 2019; Mainali et al. 2022; Sharon et al. 2022; Vanzella et al. 2022; Meštrić et al. 2023; Pascale et al. 2023) since its discovery (Dahle et al. 2016).

In this Letter, we aim to provide the clearest view thus far of the physical conditions of a LyC-leaking region by measuring the key physical properties of the Sunburst Arc on exceptionally small scales of <100 pc. By systematically comparing the physical properties of the leaking region with the nonleaking regions, we investigate whether the leaking region shows any distinct properties that might locally facilitate the escape of LyC photons. This detailed analysis is made possible through a unique combination of HST's sharp imaging and strong gravitational lensing of this exceptionally bright (integrated $m_{\mathrm{AB}} \simeq 17.5$) LyC-leaking galaxy.

Section 2 describes the observational data sets and the measurements of the physical properties (UV-continuum slope, ionization parameter, Lyα escape fraction, and equivalent width, EW, of emission lines). We present our results in Section 3 and discuss them in Section 4. We summarize our conclusions in Section 5. We adopt the ΛCDM cosmology of (H_0, Ω_m, Ω_Λ) = (70 km s^{-1} Mpc^{-1}, 0.3, 0.7) throughout the paper.

2. Observations and Data Analysis

2.1. HST Broadband and Narrowband Imaging

We analyze HST imaging of the Sunburst Arc taken as a part of several programs: GO-15101 (PI: Dahle), GO-15418 (PI: Dahle), GO-15377 (PI: Bayliss), and GO-15949 (PI: Gladders). Our analysis uses standard `Astrodrizzle` reductions of the 11 broad and medium bands published in Sharon et al. (2022) and five additional narrow bands taken from GO-15949. The narrowband data are processed using the same implementation of the `Astrodrizzle` pipeline as the other HST data from Sharon et al. (2022) and will be described in more detail in J. Rigby et al. (2023, in preparation). All imaging data were drizzled to produce final data products with a common pixel scale of 0."03. Since narrowband filters sample the continuum plus emission line flux, we also employ the associated adjacent continuum filters ("Continuum") to subtract off the continuum flux density for each line. The HST photometry used in this study appears in Table 1.

2.2. Resolving LyC Leaking and Nonleaking Regions on Small (<100 pc) Scales

The powerful combination of HST's clear imaging with a lensing magnification on the Sunburst Arc provides an effective spatial resolution down to tens of parsecs (Rivera-Thorsen et al. 2019; Diego et al. 2022; Sharon et al. 2022; Vanzella et al. 2022). The HST imaging of the Sunburst Arc reveals that only one compact star-forming region emits LyC radiation, while other parts of the galaxy do not (Rivera-Thorsen et al. 2019). The lensed galaxy images appear as four individual arcs in the sky. Across the four lensed arcs, a single leaking region is multiply lensed, resulting in 12 detectable clumps with different magnifications and lines of sight of the same physical region. Like the leaking region, the nonleaking regions of the galaxy are multiply lensed; confirmed multiple images of individual regions are described in the strong lens model (see Table 2 in Sharon et al. 2022). Images of the Sunburst Arc are shown in Figure 1. We leverage the high spatial resolution of HST to isolate the emission from the individual regions and characterize the spatially resolved physical conditions of the leaking and nonleaking regions.

2.3. UV-continuum Slope (β) Measurements

We measure the UV-continuum slope β of the multiple lensed images of the LyC-leaking region, as well as images of the nonleaking regions within the galaxy. We measure β from three HST broadband images—WFC3/UVIS F555W and

F606W and ACS/WFC F814W—that cover the rest-frame UV continuum (∼1600–2400 Å) of the galaxy at $z = 2.37$. Prior to measuring β, we correct the three bands for Milky Way reddening[13] ($E(B - V) = 0.094$) by adopting the Cardelli et al. (1989) reddening law with $R_V = 3.1$. The images are then point-spread function (PSF)–matched to the longest-wavelength data available (accounting for different spatial resolution across the available HST data, which is FWHM = 0.″15 for the reddest narrowband data).

We perform aperture photometry for individual clump images using circular apertures with a diameter of 8 pixels (=0.″24), which captures most of the emission from the largely unresolved clumps while avoiding contamination from other neighboring structures. The β is then derived by fitting the measured fluxes with the associated wavelengths for each region following the relationship (Calzetti et al. 1994)

$$f_\lambda \propto \lambda^\beta, \tag{1}$$

where f_λ is the flux density per unit wavelength (erg $\mathrm{s^{-1}\,cm^{-2}\,\AA^{-1}}$), and λ is the effective wavelength for F555W, F606W, and F814W (5308, 5887, and 8045 Å, respectively). We also measure the integrated galaxy-wide UV slope by stacking the pixels of the West Arc, which is a complete image of the whole galaxy (i.e., arc 3 in Figure 1; see also Rivera-Thorsen et al. 2019; Sharon et al. 2022). The measured UV slopes are reported in Table 2 and span a range of β values from $\simeq -2.9$ to $\simeq -2.2$.

2.4. Reddening Corrections

We compute nebular reddening corrections for the narrowband imaging data (i.e., emission line images) using the Calzetti et al. (2000) law and the average $E(B - V)_{\rm gas} = 0.195 \pm 0.025$ measured by Mainali et al. (2022) from the Hα/Hβ Balmer decrement in moderate-resolution, rest-frame optical spectra of the Sunburst Arc obtained with the Folded-port InfraRed Echellette (FIRE; Simcoe et al. 2013) spectrometer mounted on the Magellan-I Baade Telescope. The adoption of a uniform reddening correction is consistent with the conclusions of Mainali et al. (2022); they noted that there is no empirical evidence for large differences in the Balmer decrements of ground-based spectra targeting leaking versus nonleaking regions. The assumption of a uniform Balmer reddening correction is also consistent with the stellar reddening ($E(B - V)_{\rm stellar}$) derived from the far-UV spectral energy distribution (SED) modeling (Chisholm et al. 2019), which finds statistically consistent values for both the leaking and nonleaking regions (i.e., $E(B - V)_{\rm stellar}$ of 0.08 ± 0.02 versus 0.06 ± 0.01; Table 3 in Mainali et al. 2022). Interestingly, the approximate ratio of $E(B - V)_{\rm stellar}$ to $E(B - V)_{\rm gas}$ in the Sunburst Arc is also remarkably consistent with the canonical ratio (∼0.4) measured for local starburst galaxies (Calzetti et al. 2000).

It is important to note that the stellar and nebular reddening terms are estimated from ground-based observations (optical and near-IR slit spectroscopy, respectively), which include emission that is averaged over larger angular scales (i.e., ground-based seeing of ∼0.″6–0.″8) than the HST imaging that we use to measure spatially resolved UV slopes. This means that the true local reddening terms affecting spatially resolved regions within the Sunburst Arc could vary across the individual star-forming knots and partially contribute to the different UV slopes measured in leaking versus nonleaking regions. However, given the overall low reddening measured for the Sunburst Arc, spatially variable dust reddening alone cannot account for the UV slope differences measured for leaking and nonleaking regions. Assuming the maximum possible stellar reddening difference in which the isolated LyC-leaking regions are totally dust-free ($E(B - V)_{\rm stellar} = 0$) and the nonleaking regions have $E(B - V)_{\rm stellar} = 0.08$, a Reddy et al. (2016) extinction law can only produce a difference in the observed UV slope of $\Delta\beta \simeq 0.3$ (Chisholm et al. 2022; see also their Figure 5). This difference is too small to fully explain the different UV slopes measured for the leaking versus nonleaking regions in the Sunburst Arc (i.e., -2.9 ± 0.1 versus -2.2 ± 0.2; Section 3).

Table 1
HST Broadband and Narrowband Photometry Used in This Study (Section 2.1)

Instrument/Mode	Filter[a]	Exposure Time (s)	Rest-frame Features[b],[c]
WFC3/UVIS	F390W	5853	Lyα Continuum
WFC3/UVIS	F410M	13,285	Lyα
WFC3/UVIS	F555W	5616	β continuum ($\lambda_{\rm eff} \simeq 1600$ Å)
WFC3/UVIS	F606W	7878	β continuum ($\lambda_{\rm eff} \simeq 1800$ Å)
ACS/WFC	F814W	5280	β continuum ($\lambda_{\rm eff} \simeq 2400$ Å)
WFC3/IR	F126N	11,212	[O II] λ3726, 3729 Å
WFC3/IR	F128N	11,212	[O II] Continuum
WFC3/IR	F153M	5612	Hβ and [O III] Continuum
WFC3/IR	F164N	5612	Hβ
WFC3/IR	F167N	5612	[O III] λ4959 Å

Notes.
[a] In the naming convention for HST filters, the initials following the filter number are: W, broad; M, medium; and N, narrow.
[b] At the redshift of the Sunburst Arc ($z = 2.37$).
[c] "Continuum" indicates the associated adjacent filter used for continuum subtraction of each line (Section 2.5).

As we will further discuss the spatially resolved UV slope properties in Sections 4.1 and 4.2, in summary, there is extremely low internal reddening across the entirety of the Sunburst Arc, and no evidence for significant spatial variations. The uniformly small reddening affecting different lines of sight toward the Sunburst Arc indicates that differences in the stellar population ages and ISM ionization fractions are primarily responsible for the different UV slope values that we measure in spatially resolved regions within the Sunburst Arc.

2.5. Emission Line Measurements: Lyα, Hβ, [O II], and [O III]

Using the HST narrowband imaging described in Section 2.1, we measure the optical emission line ratios ([O III]/[O II] and [O III]/Hβ) and the Lyα escape fraction ($f_{\rm esc}$(Lyα)) for investigating the nebular ionization state and local Lyα escape processes, respectively, of the leaking and nonleaking regions. Measuring emission line flux requires first subtracting off the underlying continuum emission. We subtract the continuum by fitting the shape of the SED of the continuum flux density, f_λ, to all of the available HST data—except for the strongest emission line filters (i.e., F126N, F164N, and F167N as in Table 1)—of the four multiple images of the whole galaxy contained in each of arcs 1 and 2 (Figure 1)

---

[13] NASA/IPAC Galactic Dust Reddening and Extinction tool: https://irsa.ipac.caltech.edu/applications/DUST/.

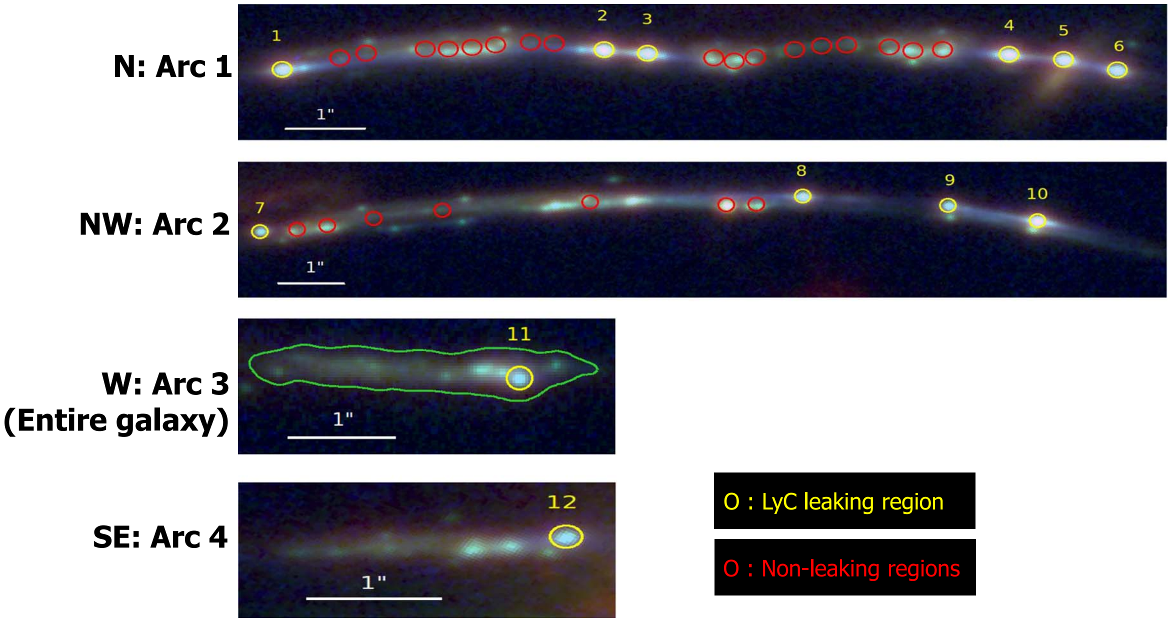

Figure 1. The HST color-composite images of the strongly lensed LyC galaxy (Sunburst Arc at $z = 2.37$), showing its spatially resolved morphology. The image filters (red: F140W; green: F606W; blue: F410M) trace the rest-frame optical, UV-continuum, and Lyα emission, respectively. The galaxy appears as four arcs due to the strong lensing effect of the foreground galaxy cluster PSZ1 G311.65–18.48 at $z = 0.44$ (Dahle et al. 2016; Sharon et al. 2022). Across the arcs, a LyC-leaking starburst region appears multiple times, as marked with yellow circles (i.e., 1–12). The lensed images of the leaking region have different lensing magnifications as computed from the lens model (Sharon et al. 2022). Each image also has a slightly different viewing angle from us. The nonleaking regions used in our analysis are marked as red circles in the arc 1 and 2 images. We also measure the galaxy-integrated physical properties from the entire galaxy region outlined in green in the arc 3 image.

pixel-wise. We feed this measured SED into the `stsynphot` and `synphot` packages (Lim 2019; STScI Development Team 2018) to compute the count rates contributed by the continuum to each filter containing an emission line, as well as its corresponding continuum filter.

Specifically, we compute the count rate corresponding to a source whose spectrum is a delta-function emission line of known flux (10^{-15} erg s^{-1} cm^{-2}). For each emission line, this results in a scaling factor to translate the measured count rate to line flux. Then, for each narrowband filter containing an emission line, we use these predicted count rates to scale the continuum filter, and we then subtract that scaled filter image from the narrowband image of the emission line. The continuum SEDs and associated narrowband filters are shown in Appendix B. The 1σ fractional uncertainties in the estimated continuum are 10%, 6%, and 6%, respectively, for Lyα, [O II], and both Hβ and [O III]; these uncertainties include both statistical and systematic sources of error in the SED fit and the continuum normalization using adjacent filters. A more detailed description of the continuum fitting and subtraction procedure will appear in a forthcoming paper (J. Rigby et al. 2023, in preparation).

We then apply Milky Way reddening corrections to the continuum-subtracted narrowband images. We also apply PSF matching to the images, with the exception of the F164N and F167N filters (Hβ and [O III], respectively), both of which are natively at the final, convolved PSF (FWHM of $0\farcs15$). Following the same aperture photometry procedure as the UV slope measurement described above (Section 2.3), we measure the key emission line fluxes (i.e., Lyα, Hβ, [O II], and [O III]) of the leaking region, the nonleaking regions, and the entire galaxy using the continuum-subtracted narrowband flux densities and the bandwidths of each filter. We also correct all emission lines, except for Lyα, for internal nebular reddening using the same Balmer decrement as in Section 2.4. Internal reddening corrections for Lyα are nontrivial due to significant resonant scattering at its line center ($\tau_0 \gg 1$), such that it is virtually impossible to correct for nebular reddening appropriately (e.g., Neufeld 1991; Verhamme et al. 2015; Dijkstra 2019). We thus do not correct Lyα emission for an internal reddening effect. Ultimately, we do not use the Lyα images to measure any line ratios that require dereddened Lyα emission.

2.6. Emission Line Ratios and Lyα Escape Fraction (f_{esc}(Lyα))

We use the emission line fluxes measured from the narrowband filters to measure several standard nebular emission line ratios, including the [O III]/[O II] line ratio, given by

$$[\text{O III}]/[\text{O II}] = \frac{[\text{O III}]5007\ \text{Å}}{[\text{O II}]3727,\ 3729\ \text{Å}}, \tag{2}$$

and the [O III]/Hβ ratio, given by

$$[\text{O III}]/\text{H}\beta = \frac{[\text{O III}]5007\ \text{Å}}{\text{H}\beta\ 4863\ \text{Å}}. \tag{3}$$

We use the [O III] λ5007 flux throughout the paper for a direct comparison of our results with the literature. The [O III] λ5007 is derived from the measured [O III] λ4959 flux by multiplying the line ratio by 2.98, which is fixed by atomic physics (Storey & Zeippen 2000).

We also measure the Lyα escape fraction ($f_{\rm esc}$(Lyα)) from the ratio of the observed to expected flux of Lyα based on the observed Hβ line flux. In practice, $f_{\rm esc}$(Lyα) is simply measured as the ratio of Lyα to Hβ multiplied by a scalar that comes from assuming Case B recombination, which means that the intrinsic Lyα flux is estimated from the hydrogen recombination physics. Specifically, we calculate the intrinsic Lyα flux by

Table 2

The Measured Properties across the Sunburst Galaxy, Showing the Distinctly Extreme Properties of the LyC-leaking Region Compared to the Nonleaking Regions and the Entire Galaxy (Section 3)

Region and ID	UV Slope (β) 1600–2400 Å	[O III]/[O II]	[O III]/Hβ	$f_{\rm esc}^{\rm Ly\alpha}$[a]	EW(Lyα)[b] (Å)	EW(Hβ)[b] (Å)	EW([O III])[b] (Å)	EW([O II])[b] (Å)
LyC-leaking[c]								
1	−2.86 ± 0.08	9.51 ± 0.81	6.77 ± 0.57	0.29 ± 0.03	48.5 ± 4.8	163.9 ± 9.8	1147.2 ± 68.8	47.4 ± 2.8
2	−2.92 ± 0.08	11.83 ± 1.00	6.89 ± 0.59	0.29 ± 0.03	43.1 ± 4.3	161.4 ± 9.7	1152.5 ± 69.1	35.7 ± 2.1
3	−2.92 ± 0.05	11.72 ± 0.99	6.57 ± 0.56	0.29 ± 0.03	39.9 ± 4.0	158.8 ± 9.5	1080.5 ± 64.8	35.1 ± 2.1
4	−2.85 ± 0.06	11.59 ± 0.98	6.77 ± 0.57	0.33 ± 0.04	42.9 ± 4.3	150.5 ± 9.0	1054.9 ± 63.3	35.3 ± 2.1
5	−2.69 ± 0.07	10.54 ± 0.89	6.75 ± 0.57	0.28 ± 0.03	42.1 ± 4.2	126.8 ± 7.6	887.1 ± 53.2	34.7 ± 2.1
6	−2.83 ± 0.07	9.13 ± 0.77	6.89 ± 0.58	0.30 ± 0.04	44.0 ± 4.4	156.8 ± 9.4	1116.2 ± 67.0	47.3 ± 2.8
8	−2.87 ± 0.07	11.15 ± 0.95	6.14 ± 0.52	0.26 ± 0.03	40.5 ± 4.0	178.9 ± 10.7	1135.0 ± 68.1	38.6 ± 2.3
9	−2.80 ± 0.07	8.38 ± 0.71	6.01 ± 0.51	0.24 ± 0.03	41.6 ± 4.2	176.7 ± 10.6	1095.0 ± 65.7	51.2 ± 3.1
10	−2.95 ± 0.08	14.62 ± 1.24	6.29 ± 0.53	0.34 ± 0.04	32.9 ± 3.3	128.7 ± 7.7	838.4 ± 50.3	21.6 ± 1.3
11	−2.67 ± 0.05	7.10 ± 0.60	5.83 ± 0.50	0.28 ± 0.03	44.2 ± 4.4	138.3 ± 8.3	830.9 ± 49.9	46.3 ± 2.8
Median[d]	−2.9 ± 0.03	10.6 ± 0.7	6.8 ± 0.1	0.3 ± 0.01	43 ± 1.3	159 ± 5.7	1095 ± 41	39 ± 2.8
Nonleaking[e]								
1	−2.16 ± 0.03	3.13 ± 0.27	4.84 ± 0.41	0.21 ± 0.03	17.5 ± 1.8	36.3 ± 2.2	180.7 ± 10.8	26.9 ± 1.6
2	−2.32 ± 0.02	3.11 ± 0.26	3.47 ± 0.29	0.22 ± 0.03	13.0 ± 1.3	34.2 ± 2.1	122.4 ± 7.3	18.5 ± 1.1
3	−2.36 ± 0.04	3.17 ± 0.27	3.50 ± 0.30	0.19 ± 0.02	9.7 ± 1.0	28.7 ± 1.7	104.0 ± 6.2	15.1 ± 0.9
4	−2.19 ± 0.00	3.50 ± 0.30	4.07 ± 0.35	0.17 ± 0.02	10.0 ± 1.0	31.4 ± 1.9	131.8 ± 7.9	18.1 ± 1.1
5	−2.22 ± 0.02	3.96 ± 0.34	4.72 ± 0.40	0.16 ± 0.02	11.2 ± 1.1	35.5 ± 2.1	173.2 ± 10.4	21.0 ± 1.3
6	−2.46 ± 0.05	4.72 ± 0.40	4.23 ± 0.36	0.07 ± 0.01	4.3 ± 0.4	37.8 ± 2.3	165.0 ± 9.9	15.2 ± 0.9
7	−2.15 ± 0.00	3.34 ± 0.28	4.44 ± 0.38	0.10 ± 0.01	9.3 ± 0.9	52.6 ± 3.2	240.1 ± 14.4	33.7 ± 2.0
8	−2.25 ± 0.01	3.51 ± 0.30	4.25 ± 0.36	0.11 ± 0.01	11.5 ± 1.1	52.7 ± 3.2	230.6 ± 13.8	30.3 ± 1.8
9	−2.39 ± 0.00	5.21 ± 0.44	4.71 ± 0.40	0.13 ± 0.02	7.2 ± 0.7	39.6 ± 2.4	192.4 ± 11.5	15.3 ± 0.9
10	−2.33 ± 0.03	4.46 ± 0.38	4.21 ± 0.36	0.22 ± 0.03	14.8 ± 1.5	38.0 ± 2.3	165.6 ± 9.9	17.2 ± 1.0
11	−1.89 ± 0.00	3.45 ± 0.29	5.61 ± 0.48	0.25 ± 0.03	63.4 ± 6.3	108.7 ± 6.5	623.2 ± 37.4	77.7 ± 4.7
12	−2.03 ± 0.03	3.26 ± 0.28	3.91 ± 0.33	0.18 ± 0.02	46.1 ± 4.6	91.1 ± 5.5	364.9 ± 21.9	52.7 ± 3.2
13	−1.96 ± 0.00	3.55 ± 0.30	4.82 ± 0.41	0.25 ± 0.03	59.8 ± 6.0	90.9 ± 5.5	448.0 ± 26.9	56.5 ± 3.4
14	−1.88 ± 0.05	3.37 ± 0.29	5.32 ± 0.45	0.24 ± 0.03	88.0 ± 8.8	152.6 ± 9.2	826.8 ± 49.6	105.4 ± 6.3
15	−2.03 ± 0.01	2.86 ± 0.24	4.57 ± 0.39	0.04 ± 0.00	13.0 ± 1.3	129.5 ± 7.8	597.3 ± 35.8	112.0 ± 6.7
16	−2.12 ± 0.02	2.94 ± 0.25	3.82 ± 0.32	0.04 ± 0.00	18.0 ± 1.8	158.0 ± 9.5	605.9 ± 36.4	89.3 ± 5.4
17	−2.09 ± 0.02	2.79 ± 0.24	4.37 ± 0.37	0.06 ± 0.01	18.8 ± 1.9	116.3 ± 7.0	514.2 ± 30.9	85.9 ± 5.2
18	−1.87 ± 0.00	4.81 ± 0.41	5.21 ± 0.44	0.13 ± 0.02	17.6 ± 1.8	41.3 ± 2.5	222.2 ± 13.3	23.0 ± 1.4
19	−2.31 ± 0.06	2.37 ± 0.20	3.41 ± 0.29	0.12 ± 0.01	4.3 ± 0.4	22.1 ± 1.3	77.6 ± 4.7	15.3 ± 0.9
20	−2.09 ± 0.02	3.66 ± 0.31	3.44 ± 0.29	0.08 ± 0.01	37.0 ± 3.7	112.0 ± 6.7	390.7 ± 23.4	48.5 ± 2.9
21	−1.86 ± 0.01	3.10 ± 0.26	4.21 ± 0.36	0.04 ± 0.00	12.5 ± 1.2	111.1 ± 6.7	474.1 ± 28.4	69.2 ± 4.2
22	−2.23 ± 0.01	3.35 ± 0.28	4.61 ± 0.39	0.15 ± 0.02	10.5 ± 1.0	36.2 ± 2.2	172.1 ± 10.3	24.9 ± 1.5
23	−2.64 ± 0.10	1.79 ± 0.15	4.01 ± 0.34	0.09 ± 0.01	4.2 ± 0.4	31.0 ± 1.9	128.9 ± 7.7	61.6 ± 3.7
24	−2.50 ± 0.06	5.51 ± 0.47	4.82 ± 0.41	0.11 ± 0.01	6.8 ± 0.7	46.2 ± 2.8	229.3 ± 13.8	17.3 ± 1.0
Median[c]	−2.2 ± 0.04	3.4 ± 0.18	4.4 ± 0.12	0.13 ± 0.01	13 ± 4.4	46 ± 8.8	229 ± 42	30 ± 6.4
Entire galaxy[f]	−2.20 ± 0.03	3.81 ± 0.32	4.80 ± 0.41	0.14 ± 0.02	33.1 ± 3.3	103.8 ± 6.2	503.5 ± 30.2	55.7 ± 3.3

Notes.

[a] The Lyα escape fraction measured in Section 2.6, assuming Case B recombination.

[b] Rest-frame EW.

[c] The multiple images of the leaking region as identified in Figure 1. The associated R.A. and decl. are listed in Table 3.

[d] The reported uncertainties are the standard error of the mean of the measured parameters (i.e., divided by $\sqrt{N}$).

[e] The nonleaking regions as identified in Figure 1. The associated R.A. and decl. are listed in Table 3.

[f] The entire galaxy (arc 3) as identified in green in Figure 1.

multiplying the Hβ flux by 23.3, which is the appropriate scaling factor for Case B recombination for an electron temperature $T_{\rm e} = 10{,}000$ K and an electron number density $n_{\rm e} = 100\,{\rm cm}^{-3}$ (Dopita & Sutherland 2003). While the definition of $f_{\rm esc}$(Lyα) adopted in this paper is consistent with the literature, it should be noted that our $f_{\rm esc}$(Lyα) is measured on scales of resolved star-forming regions within a galaxy (e.g., Wofford et al. 2013; Rivera-Thorsen et al. 2015). This differs from the $f_{\rm esc}$(Lyα) measured based on the entire galaxy in the literature (e.g., Henry et al. 2015; Yang et al. 2017). Thus, our $f_{\rm esc}$(Lyα) measured from the resolved star-forming regions should be considered the "local" line-of-sight observed Lyα escape fraction rather than the global galaxy property.

2.7. Hβ Flux Calibration

Comparing our measurements to other observations of the Sunburst Arc, including the ground-based spectroscopy presented in Mainali et al. (2022), as well as unpublished HST WFC3/IR G141 grism spectroscopy (PID: 15101; J. Rigby et al. 2023, in preparation), we find that the Hβ flux measured from the F164N WFC3/IR filter is systematically ∼60% lower than other measurements of the same emission line in spectra taken with both Magellan/FIRE and the WFC3/IR G141 grism (J. Rigby 2023, in preparation). This offset is much larger than the statistical and systematic uncertainties in the measured F164N Hβ flux and cannot be explained by any treatment of the continuum subtraction (i.e., a large negative continuum flux density, which is nonphysical, would be required to bring F164N into agreement with the WFC3/IR grism). The large difference between narrowband and grism Hβ fluxes is especially puzzling considering that F164N and the G141 grism are part of the same WFC3/IR instrument and calibration pipeline. After a thorough exploration of all possible systematic, reduction, and analysis effects, we conclude that the calibration data available in the WFC3/IR pipeline for F164N—a scarcely used narrowband filter—is likely out of date, and that the filter throughput either was not correctly calibrated or has substantially degraded since the most recent calibration observations were taken. Therefore, we ad hoc increase all Hβ flux measurements by 60% to account for this uncertainty.

It is important to note that this correction does not qualitatively change our comparison of the emission line properties of the leaking versus nonleaking regions because it is applied uniformly to the entire F164N image and therefore shifts the measured line ratio of [O III]/Hβ and $f_{\rm esc}$(Lyα) and EW of Hβ (EW (Hβ)) in the same direction.

2.8. Emission Line EWs

The emission line fluxes and underlying continuum flux density measurements described above can also be used to measure the EW of the nebular emission lines. We compute the observed-frame $\rm EW_{obs}$ of each emission line by dividing the attenuation-uncorrected line flux by the underlying continuum flux density (assumed to be constant) and then compute the rest-frame EW as $\rm EW_{rest} = EW_{obs}/(1 + \mathit{z})$. The resulting emission line EW values are useful for contextualizing the EW properties of the clumps (i.e., the leaking and nonleaking regions) we observe in the Sunburst Arc with other extreme star-forming galaxies in the literature.

3. Results

Our analysis pins down the properties of the LyC-leaking region on small scales of <100 pc within a galaxy. Specifically, we compare the relationships between the UV slope β, the ionization-sensitive line ratios [O III]/[O II] and [O III]/Hβ, and Lyα escape fraction $f_{\rm esc}$(Lyα) for individual resolved regions within the Sunburst Arc, as well as for the entire galaxy. Due to contamination from a foreground galaxy associated with an intervening absorption system (Lopez et al. 2020) and a foreground star, images 7 and 12 of the leaking region are excluded in this analysis. All measurements are reported in Table 2.

It is noteworthy that all of the presented parameters are lensing magnification–independent, as they are intrinsically the ratio of measured parameters, which means that the lensing magnification cancels out. Rather, what the lensing magnification uniquely provides in our analysis is the spatially resolved morphology of the Sunburst Arc on small scales sufficient to isolate the leaking region from the nonleaking regions (see Sharon et al. 2022, for further details about the lens model).

3.1. Very Blue UV Slope and High Ionization State of the LyC-leaking Region

This analysis constrains, for the first time at any redshift, the UV slope β, as well as the [O III]/[O II] and [O III]/Hβ line ratios, of a spatially resolved, leaking star-forming region within a galaxy (rather than galaxy-integrated). The individual images of the leaking region show a distinctly blue UV-continuum slope and high ionization compared to any other nonleaking regions within the galaxy. This trend is shown in Figure 2, where it is clear that the multiply lensed leaking region (the numbered black points in the figure) occupies the parameter space of a very blue UV slope ($\beta = -2.9 \pm 0.1$) and high ionization ([O III]/[O II] $= 11 \pm 3$ and [O III]/Hβ $= 6.8 \pm 0.4$). This is in stark contrast to the nonleaking regions (i.e., the red points), which show a systematically redder UV slope ($\beta \simeq -2.2$) and lower ionization state ([O III]/[O II] $\simeq 4$, [O III]/Hβ $\simeq 4$).

These extreme values of β and [O III]/[O II] of the leaking region significantly ($\gtrsim 7\sigma$) deviate from the nonleaking regions, which have β and [O III]/[O II] of -2.2 ± 0.2 and 4 ± 0.6, respectively. Also, a comparison with the whole galaxy-integrated β of -2.2 ± 0.03 and [O III]/[O II] of 4 ± 0.3 (i.e., represented by the blue diamond in Figure 2) shows that the UV slope and ionization state of the leaking region are indeed extreme relative to the galaxy as a whole.

3.2. Blue UV Slope versus High Lyα Escape from the LyC-leaking Region

Plotting β and $f_{\rm esc}$(Lyα) for all measured regions within the Sunburst Arc (i.e., left panel of Figure 3) reveals a consistent separation between the LyC-leaking region and the other regions of the galaxy. The blue β and high $f_{\rm esc}$(Lyα) of the leaking region are clearly distinct from the redder β and lower $f_{\rm esc}$(Lyα) of the nonleaking regions, and there is a broad anticorrelation between β and $f_{\rm esc}$(Lyα). We measure the typical $f_{\rm esc}$(Lyα) for the leaker and nonleakers of 0.3 ± 0.03 and 0.13 ± 0.07, respectively. Also similar to what we saw with β and the [O III]/[O II] and [O III]/Hβ ratios, the galaxy-integrated $f_{\rm esc}$(Lyα) (0.14 ± 0.02) matches the nonleaker values.

Although the absolute values of $f_{\rm esc}$(Lyα) in this paper are subject to a systematic uncertainty resulting from the problematic Hβ narrowband imaging flux calibration (Section 2.7), we note that the trend of the higher $f_{\rm esc}$(Lyα) of the leaking region than the nonleaking regions (i.e., Figure 3) does not change because the flux offset applies to all regions of the galaxy.

3.3. High Lyα Escape Fraction versus High Ionization State for the LyC-leaking Region

The relationships between $f_{\rm esc}$(Lyα) and ionization state ([O III]/[O II]) within the Sunburst Arc reveal a consistent picture about the distinctly extreme properties of the leaking region as in the preceding sections. The right panel of Figure 3 shows that the leaking region occupies the parameter space of high $f_{\rm esc}$(Lyα) and [O III]/[O II], while the nonleaking regions have low $f_{\rm esc}$(Lyα) and [O III]/[O II]. The galaxy-integrated

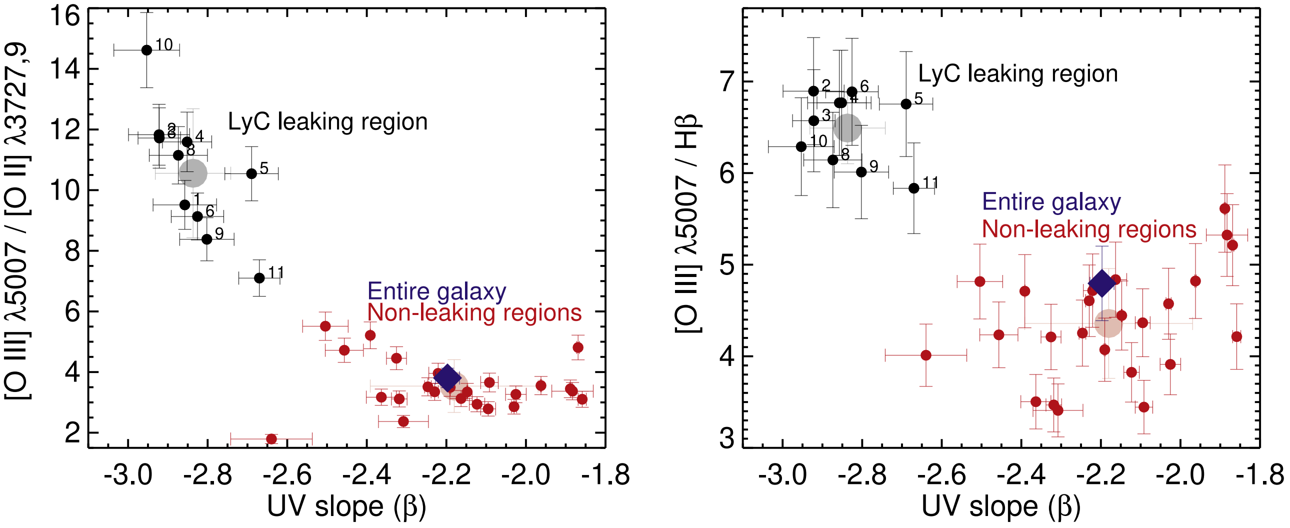

Figure 2. Left: [O III]/[O II] vs. UV-continuum slope (β) for the leaking region (black), the nonleaking regions (red), and the entire galaxy (blue) as marked in Figure 1. The light gray and pink circles with error bars indicate the mean value and 1σ population deviation of each region. Right: same as the left panel but for [O III]/Hβ. In the Sunburst Arc, the multiple lensed images of the LyC-leaking region (black) show the remarkably blue UV-continuum slope $\beta \simeq -2.9$ and the high ionization state of the surrounding ISM ([O III]/[O II] $= 11 \pm 3$ and [O III]/H$\beta = 6.8 \pm 0.4$), which is distinctly extreme compared to the nonleaking regions (red) and the entire galaxy (blue). The leaking region's extremely blue β and high ionization–sensitive line ratios (corresponding to an ionization parameter $\log U$ of $\simeq -2$; Section 4.1) suggest that LyC photons are produced and escape from a local, highly ionized compact region with extreme stellar populations (Section 4).

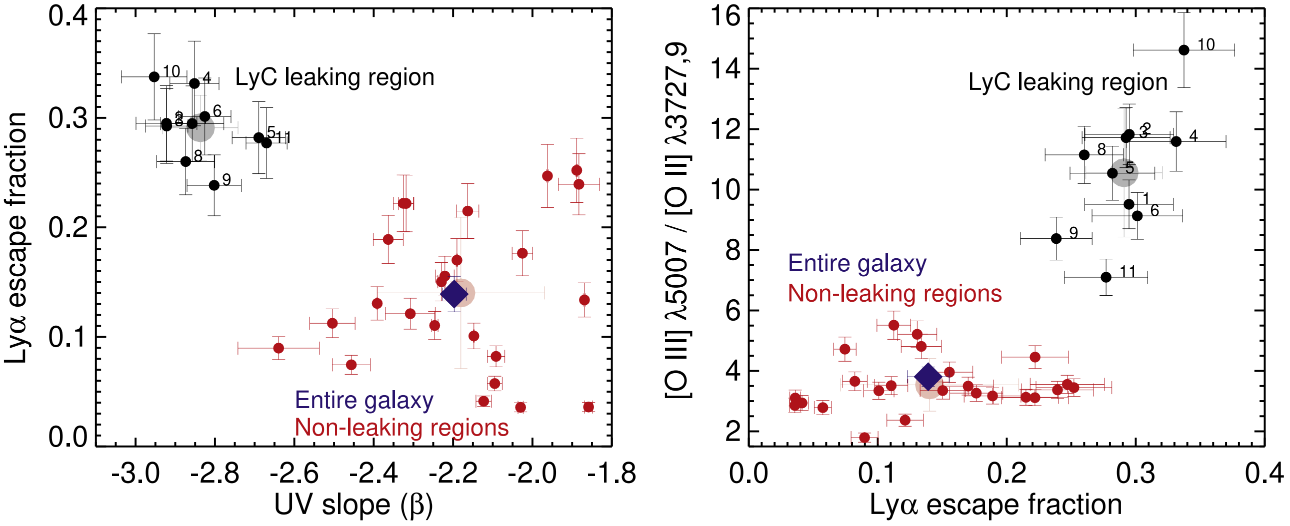

Figure 3. Lyα escape fraction ($f_{\rm esc}$(Lyα)) vs. β (left) and [O III]/[O II] vs. $f_{\rm esc}$(Lyα) (right) relations for the leaking region, the nonleaking regions, and the entire galaxy. The format is the same as in Figure 2. Combined with the very blue β and high [O III]/[O II] ratio, the leaking region is clearly characterized by relatively high $f_{\rm esc}$(Lyα), the presence of extreme stellar populations, and a highly ionized nebular state (Sections 4.1 and 4.2). It also implies a physical connection between LyC and Lyα escape processes on subkiloparsec scales such that the LyC-leaking region features a higher escape fraction of Lyα as well, likely due to the preferred low N(H I) channels for both photons (Section 4.3).

values are consistent with those of the nonleaking regions. This trend of a high Lyα escape fraction and high ionization of the leaking region condenses the relations seen in the left panels of Figures 2 and 3 showing that the UV slope tracks closely with both the ionization state (Figure 2) and $f_{\rm esc}$(Lyα) (Figure 3) by directly relating the ionization state with $f_{\rm esc}$(Lyα).

This result makes physical sense, with the right panel of Figure 3 clearly showing that the escape of Lyα is typically related to the nebular ionization state on the scale of star-forming clumps, such that Lyα photons locally escape more easily from the highly ionized star-forming regions than the low-ionization regions. We also note that the galaxy-integrated $f_{\rm esc}$(Lyα) and [O III]/[O II] look like the resolved nonleaking regions, all of which have $f_{\rm esc}$(Lyα) and ionization properties that are broadly consistent with those observed in low-redshift green pea galaxies (e.g., Yang et al. 2017; Flury et al. 2022a). Additionally, while the interpretation of the relation between the escape of Lyα photons and the nebular ionization state makes physical sense overall, it should also be noted that the actual physical correlations may be more complex, in the sense that a high $f_{\rm esc}$(Lyα) region does not always correspond to a high [O III]/[O II] region (e.g., Haro 11; Keenan et al. 2017; Östlin et al. 2021).

3.4. High EW Emission Lines of the LyC-leaking Region

The LyC leakers are often characterized by the high EW of the emission lines (notably, Lyα, Hβ, [O III] λ5007, and [O II]

λ3727, 3729; e.g., Izotov et al. 2016b, 2018b). We see the same qualitative relationship between emission line EW and LyC leakage, notably on subgalactic scales in the emission line EWs of the leaking region, the nonleaking regions, and the entire Sunburst Arc galaxy (Table 2). The median EWs of the leaking region are typically a factor of 2−5 (depending on which specific line is compared) higher than those of the nonleaking regions. The EW values measured for the entire integrated galaxy emission are similar to those of the nonleaking region. This is to be expected because the leaking region is only a very small part of the galaxy (∼17% of the UV-continuum light), while the nonleaking regions dominate the galaxy.

Consistent with previous results about bluer UV slope, higher ionization state, and higher Lyα escape fraction (Sections 3.1, 3.2, and 3.3), the higher emission line EWs of the leaking region suggest that ionizing photons escape from a specific star-forming region with extreme physical properties inside the galaxy.

4. Discussion

4.1. Extreme Properties of the Compact (<100 pc) LyC-leaking Region

Our key result is that the LyC-leaking region within the Sunburst Arc has dramatically different properties than the rest of the galaxy. The LyC-leaking clump is an extremely compact star-forming region with a very blue UV-continuum slope ($\beta \sim -2.9$), high ionization (i.e., [O III]/[O II] ∼ 11), high Lyα escape fraction ($f_{\rm esc}$(Lyα) ∼ 0.3), and high oxygen EW([O III]) ∼ 1100 Å (Figures 2 and 3 and Table 2). The LyC-leaking region is only a small unresolved (<100 pc) piece of the entire galaxy (Figure 1), and it exhibits physical conditions that are clearly most extreme over all other (nonleaking) star-forming regions.

Morphologically, such a compact shape of the leaking region seems related to the presence of dense star clusters and suggests the importance of concentrated star formation to the escape process of LyC radiation. Indeed, (nonlensed) LyC leakers exhibit markedly similar compact star formation at all redshifts ($0.02 < z < 3.5$; e.g., Bergvall et al. 2006; Borthakur et al. 2014; Izotov et al. 2016a, 2018a; Vanzella et al. 2016). Due to the concentrated star formation, the leakers show a high star formation surface density, $\Sigma{\rm SFR} \gtrsim 1\ M_\odot\ {\rm yr}^{-1}\ {\rm kpc}^{-2}$ (Izotov et al. 2016a, 2018a; Kim et al. 2020, 2021; Flury et al. 2022a), and a significant correlation between the LyC escape fraction and UV-continuum size (Flury et al. 2022b).

Unsurprisingly, we also see a markedly high ionization state of the gas (i.e., based on a high [O III]/[O II] of ≃11 and [O III]/H$\beta \simeq 7$; Figure 2) of the leaking region. A well-known tracer for the ionization state of the gas (e.g., Kewley & Dopita 2002; Nakajima & Ouchi 2014; Kewley et al. 2019; Nakajima et al. 2022), the [O III]/[O II] line ratio of ≃11 corresponds to a very high ionization parameter of $\log U \simeq -2$ based on the photoionization models of Kewley et al. (2019) and Nakajima et al. (2022) using the best-fit metallicity of 0.5 $Z_\odot$ for the leaking region (Chisholm et al. 2019). The high $\log U \simeq -2$ strongly indicates the presence of highly ionized, low N(H I) along the line of sight toward the leaking region.

Such a high ionization parameter of the leaking region is notably comparable to those of "super star clusters" found in the local Universe (e.g., Indebetouw et al. 2009; James et al. 2016; Micheva et al. 2017, 2019; Leitherer et al. 2018). Given the high ionization parameter and the intrinsically small size ($r \lesssim 50$ pc) of the leaking region after correcting for lensing magnification (Sharon et al. 2022; Vanzella et al. 2022), it is very likely that the leaking region harbors an actively forming super star cluster(s).

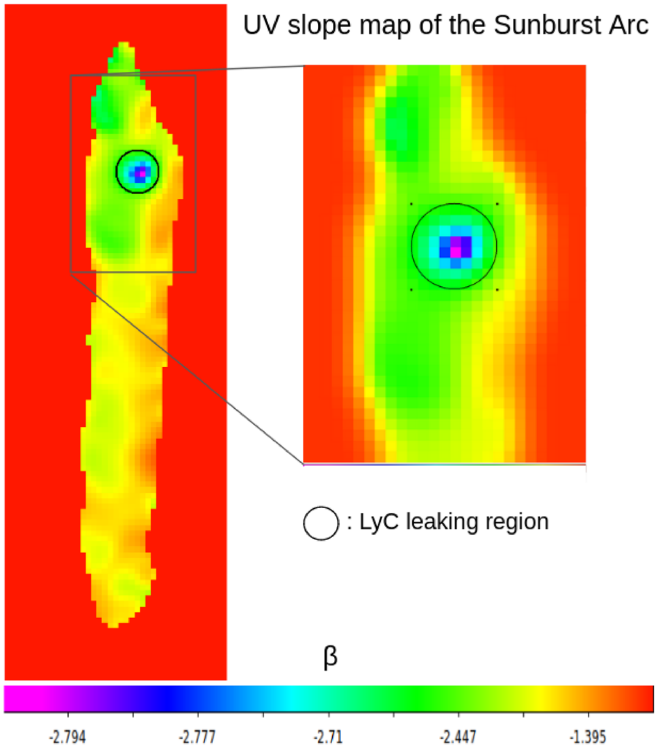

Figure 4. The UV slope map of the entire galaxy (i.e., "arc 3" in Figure 1). The zoom-in view of the leaking region shows the distinctly blue UV slope of the leaking region compared to any other nonleaking regions of the galaxy. Consistent with previous figures, the β map suggests that the escape of LyC photons in the Sunburst Arc is primarily driven by a local, compact starburst region that is likely harboring a young star cluster(s) (Section 4.1).

These extreme properties of the leaking region are remarkably consistent with other, previously analyzed properties of the leaking region, such as the strong, highly ionized gas outflows (Mainali et al. 2022), as well as the triple-peak profile of the Lyα emission line (Rivera-Thorsen et al. 2017). All of these properties of the leaking region show a coherent picture of a LyC escape mechanism where LyC photons escape from a particular extremely star-forming compact region (e.g., super star clusters) within a galaxy, rather than the entire galaxy. Such a localized LyC escape process is also consistent with the trend shown in the UV slope map of the entire Sunburst galaxy (using the "arc 3" image) in Figure 4, where the leaking region distinctly features very blue β, unlike other nonleaking regions.

4.2. Small Ionized Channels for the Escape of LyC and Nearly "Pure" Stellar Light

The leaking region's UV-continuum slope ($\beta = -2.9 \pm 0.1$; Figure 2) is extremely blue compared to the typical slopes ($-2.5 \lesssim \beta \lesssim 0$) found in star-forming galaxies across redshifts ($0 < z < 9$; e.g., Meurer et al. 1999; Hathi et al. 2008; Bouwens et al. 2010; Dunlop et al. 2012; Reddy et al. 2018; Bhatawdekar & Conselice 2021; Chisholm et al. 2022; Topping et al. 2022). How could such blue $\beta \simeq -3$ be produced in the leaking region? Theoretically, the very blue

UV slope indicates the presence of extreme stellar populations characterized by little/no dust, a young age, and low metallicity with a high ionizing photon escape fraction (Leitherer et al. 1999; Schaerer 2003; Zackrisson et al. 2013; Chisholm et al. 2022; Marques-Chaves et al. 2022). This would mean that ionizing photons are produced from young, hot O (and late B-type) stars, and the photons escape through empty space with little dust to avoid dust obscuration. Therefore, the leaking region's β of -2.9 seems to strongly indicate that we are seeing the uninterrupted "pure" UV stellar light of these ionizing hot stars from the leaking region.

Indeed, the comparison of the leaking region's UV slope with the modeled slopes for low-metallicity young stellar populations (Schaerer 2003) shows that their slopes are markedly consistent within the uncertainties. The leaking region's $\beta = -2.9 \pm 0.1$ closely matches with the modeled βs for subsolar metallicity ($Z = 0.4\ Z_{\odot}$), young ($\lesssim$5 Myr) stellar populations as shown in Figure 5. Furthermore, the comparison shows that only the most extreme models containing approximately "pure" stellar light—i.e., minimal contribution of nebular continuum emission—are still able to predict β values that match with the observed β of the leaking region. We checked that even for very low metallicity starburst population models (0.02–0.2 $Z_{\odot}$) only "pure" stellar light models are able to predict the blue βs comparable to that of the leaking region. Such remarkable agreement in UV slopes between the leaking region and the "pure" stellar light models suggests that there is an exceptionally low H I column density channel through which the unabsorbed "direct" stellar light, including LyC photons, is able to escape without interruption by neutral hydrogen gas and dust contents.

These results point to a physical picture in which strong stellar feedback by a cluster of massive stars in the leaking region creates some highly ionized cavities of low neutral hydrogen and/or little dust. Through these "pencil-beam" cavities, "direct" stellar light, including LyC photons, is able to escape into the IGM. The cavities would also help Lyα photon escape by reducing the scatterings with the surrounding gas, in agreement with the higher $f_{\rm esc}$(Lyα) (Figure 3) and the presence of central, narrow Lyα peak profiles (Rivera-Thorsen et al. 2017) in the leaking region than in the nonleaking regions. In this viewing geometry, we may be staring "down the barrel" of the inner hot H II region surrounding the ionizing star cluster; in that inner H II region, highly ionized gas produces strong emission lines (such as [O III]), while nebular continuum is relatively weak as gas is mostly ionized suggesting that the free-bound process is unlikely to contribute to the nebular continuum (Mollá et al. 2009). Without the extremely high magnification from strong lensing we would be not be able to separate the leaking region from the nonleaking regions and pin down this specific escape channel(s). We will further discuss the viewing geometry of LyC escape in Section 4.4.

4.3. LyC Escape Tracks with Lyα Escape on Subgalactic Scales in the Sunburst Arc

The escape of Lyα photons is one of the most compelling indirect indicators for LyC leakage (e.g,. Behrens et al. 2014; Verhamme et al. 2015; Rivera-Thorsen et al. 2017; Izotov et al. 2021; Kimm et al. 2022). Both Lyα and LyC photons require low column density H I gas to escape, although the precise escape fractions of Lyα and LyC photons are expected to substantially differ due to the larger interaction cross section of Lyα with H I atoms, a consequence of the resonant scattering nature of Lyα photons (e.g., Neufeld 1991; Gronke et al. 2016). Consistent with these expectations, we find that the leaking region shows higher $f_{\rm esc}$(Lyα) compared to the nonleaking regions; the mean $f_{\rm esc}$(Lyα) of the leaking and nonleaking regions are 0.3 ±0.03 and 0.13 ±0.07, respectively (Figure 3 and Table 2). Note that $f_{\rm esc}$(Lyα) here is measured on individual star-forming region scales and thus should be interpreted as a "local" line-of-sight Lyα escape fraction, as described in Section 2.6.

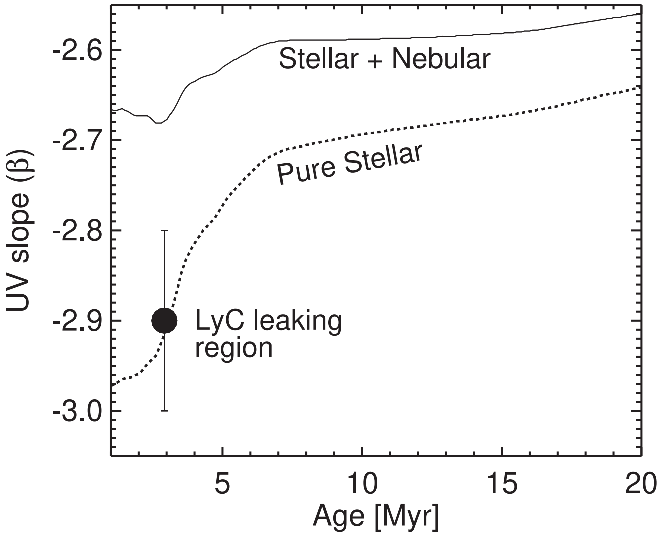

Figure 5. The comparison of the leaking region's UV slope with starburst population models suggests that the leaking region's UV light is dominated by "pure" stellar light (i.e., minimal contribution from nebular continuum emission and extinction by dust). The age (∼3 Myr) of the leaking region is adopted from the far-UV SED modeling in Chisholm et al. (2019). Both the "stellar+nebular" and "pure stellar" models assume the same constant star formation history and subsolar metallicity of 0.4 $Z_{\odot}$, which is similar to the metallicity derived from Chisholm et al. (2019). The starburst population models are adopted from Schaerer (2003). The leaking region's β, consistent with the "pure stellar" model, suggests that the leaking region's UV emission nearly exclusively consists of uninterrupted direct starlight, with minimal contributions from nebular continuum emission and negligible dust extinction. Such direct starlight from the leaking region indicates the presence of small ionized channels through which LyC photons escape (Section 4.2).

It is especially interesting to see in the Sunburst Arc that both the $f_{\rm esc}$(Lyα) and LyC escape fraction vary dramatically on subgalactic scales. This reinforces the fact that geometric factors such as low H I gas channels along the line of sight are critically important to the escape mechanisms for both. Ongoing investigations of the Lyα emission profiles of the leaking and nonleaking regions in the Sunburst Arc will further elucidate the interdependence between LyC and Lyα escape mechanisms (Owens et al. and Rivera-Thorsen et al. 2023, in preparation).

4.4. The Viewing Geometry for LyC Escape from Star Clusters

The Sunburst Arc is a clear example of a LyC escape process that is driven by a specific compact star-forming region within a galaxy. The compact and vigorously star-forming region is harboring a super star cluster considering its small, compact size with extreme properties (Figures 2 and 3 and Table 2). The super star cluster (1) produces an enormous amount of ionizing photons and (2) likely plays a key role in enabling the photons to escape into the IGM through specific lines of sight where there is little nebular continuum emission and dust screening.

These unique insights into the locally regulated (i.e., not galaxy-wide) LyC escape processes by a prominent star cluster are only achievable by accurately pinning down the particular region of LyC leakage within the galaxy. Such observations require the unique combination of a strongly gravitationally lensed LyC leaker (such as the Sunburst Arc) and the sharp angular resolution of HST.

The multiple lensed images of the leaking region (i.e., the numbered knots in Figure 1) also allow us to investigate whether the escape of LyC is directional or isotropic (i.e., the viewing geometry). Even among the separate lensed images of the LyC-leaking region in the Sunburst Arc, we see significant scatters among both the physical properties (i.e., Figures 2 and 3) and the LyC escape fraction (Rivera-Thorsen et al. 2019). From the lens model of the system, we know that the gravitational deflection that produces each of these lensed images results in a slightly different viewing angle and a different magnification factor for each image (see Figures 7 and 14 in Sharon et al. 2022). Thus, the variations in the physical properties measured from the lensed images indicate that the geometry of the leaking region is very likely anisotropic, such that its measured properties depend on which line of sight we look through (e.g., patchy H I clouds and cavities in the ISM).

There are substantial variations among the properties measured from the leaking region's lensed images (i.e., the scattered distribution of the black data points in Figures 2 and 3). The variations in β ($-3\lesssim\beta\lesssim -2.7$), [O III]/[O II] ($7\lesssim$ [O III]/[O II] $\lesssim 15$), and $f_{\rm esc}$(Lyα) ($0.25\lesssim f_{\rm esc}$(Lyα) $\lesssim 0.35$) are larger than the measurement uncertainties and likely related to the details of lensing configuration, including slightly different viewing geometries and different lensing magnifications of the leaking region images. Qualitatively, we see trends between the variations in the physical properties and lensing magnification such that highly magnified images (e.g., clumps 10 and 2) tend to show more extreme properties, such as a bluer UV slope and higher [O III]/[O II] ionization state.

This is consistent with the leaking LyC radiation emerging from a narrow, pencil-beam channel that is, at best, barely resolved. In this physical picture, some lensed images provide a cleaner view of the escape channel, while at the same time, the more highly magnified images provide a cleaner, better-isolated view of the LyC-leaking line of sight than the lower-magnification images, which are likely more blended with surrounding nonleaking regions. A quantitative assessment of these lensing effects requires a careful forward-modeling analysis, which is beyond the scope of this paper.

The systematic variations found in this study clearly suggest that the structure of the LyC-leaking region and the associated LyC escape process is highly directional (anisotropic) depending on a specific line of sight. This means that we are viewing the galaxy from a very privileged vantage point through pencil-beam channels. If we had viewed it from most other angles, we may not have see ionizing escape. Such anisotropic viewing geometry for LyC escape in the Sunburst Arc is illustrated in Figure 6. While the LyC escape fraction along our line of sight is very high, ∼40%, the galaxy-integrated global escape fraction is likely lower considering the small projected area of the leaking region within the galaxy. Combined with such privileged sight lines, the global escape fraction is on the order of 5% given that the leaking region accounts for ∼17% of the galaxy's nonionizing UV-continuum light (based on the F555W flux). If the pencil-beam viewing geometry seen in the Sunburst Arc is a common way of escaping in star-forming galaxies, it is likely that field searches are missing substantial populations of LyC leakers for which the leaking channels are misaligned with our viewing angle.

4.5. Implications for Reionization

One clear implication of our analysis is that the LyC escape process is a highly local process, and individual young, dense star clusters play a key role in facilitating the escape of LyC photons. The unique magnified view of LyC leakage provided in the Sunburst Arc reveals that one such LyC-leaking star cluster is characterized by an extremely blue UV slope and high ionization state, while the nonleaking regions of the galaxy have properties consistent with a typical star-forming galaxy. In fact, the integrated, galaxy-averaged properties can be quite unremarkable, as demonstrated by the integrated properties measured for the Sunburst Arc using the low-magnification complete image of the galaxy ("arc 3" in Figure 1 and the blue diamonds in Figures 2 and 3).

A second implication is that LyC escape is, in at least some cases, a highly anisotropic process (i.e., Figure 6). The extreme physical conditions that are associated with LyC escape only occur across a very small fraction of the surface of the Sunburst Arc, implying that the ionizing radiation is escaping through channels that subtend a very small solid angle (i.e., through channels that are long and thin). If pencil-beam channels are a common mode of LyC escape, then it follows that detecting LyC escape from any single galaxy will likely be strongly viewing angle–dependent, such that measurements of LyC escape in individual galaxies cannot safely be used to measure the volume-averaged escaping ionizing radiation due to viewing angle effects.

We can draw two important conclusions about LyC-leaking galaxies: (1) their galaxy-integrated properties need not be extreme, and (2) their escaping LyC radiation is likely to be highly anisotropic and viewing geometry–dependent (i.e., favorable sight lines). The combination of locally regulated LyC escape mechanisms by super star clusters and pencil-beam geometries for channels of escaping ionizing radiation implies that it should be quite difficult to draw robust conclusions about galaxies' escaping LyC radiation using indirect indicators based on integrated, galaxy-averaged properties. Notably, these pencil-beam channels driven by small, individual star clusters provide a natural explanation for why studies analyzing the integrated galaxy properties associated with LyC escape have found significant scatters (or weak trends) between those integrated galaxy properties and the LyC escape fraction (e.g., Chisholm et al. 2018; Izotov et al. 2021; Flury et al. 2022a; Saldana-Lopez et al. 2022; Saxena et al. 2022; Seive et al. 2022).

5. Summary and Conclusions

We investigate the physical conditions for LyC escape by isolating and measuring the key properties of a leaking region in a strongly lensed LyC emitter at $z = 2.37$ (aka the Sunburst Arc). Thanks to high magnification from strong lensing, this galaxy reveals the exceptionally small-scale (tens of parsecs) physics of LyC escape; its lensing-magnified images reveal that only one compact star-forming region emits ionizing photons, while the other regions do not (Figure 1). Analyzing the HST's sharp images (Table 1 and Figure 7), we spatially resolve the properties

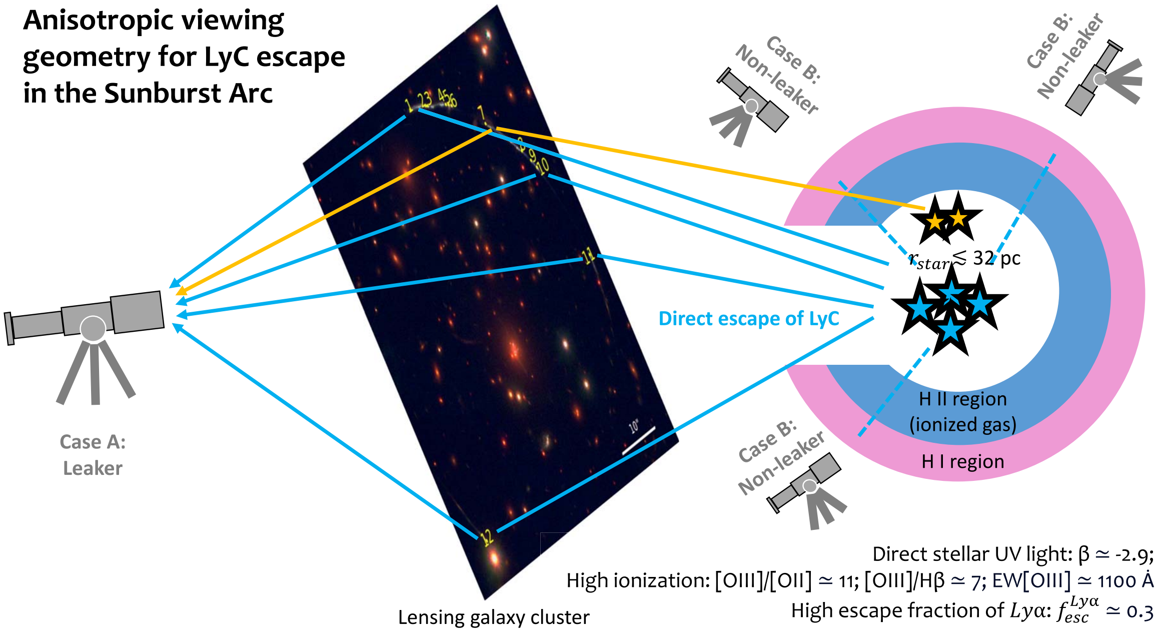

Figure 6. Illustrative diagram of the anisotropic viewing geometry for LyC escape in the Sunburst Arc. Case A is the pencil-beam viewing geometry suggested for the galaxy, where LyC photons directly escape from the ionizing star cluster through a highly ionized, low N(H I) hole(s) that opens toward our line of sight. In this viewing geometry, we may be staring "down the barrel" of the inner hot H II region of the ionizing star cluster, enabling us to observe LyC photons and pristine stellar light that are minimally attenuated by neutral hydrogen and dust, as indicated by the very blue $\beta \simeq -2.9$ of the leaking region (Section 4.4). This anisotropic LyC escape process through specific opening angles implies that if we view the galaxy from most other angles, we may not see escaping ionizing photons and thus might identify it as a nonleaker, which is depicted as case B. Thanks to strong lensing magnification, our analysis isolates the physical properties of the leaking region (blue stars) from the nonleaking regions (orange stars). The size ($r_{\rm star} \lesssim 32$ pc) of the ionizing star cluster is an upper limit due to the HST's spatial resolution and is estimated from the strong lens model analysis of Sharon et al. (2022).

of the leaking region (<100 pc) and compare with the nonleaking regions, as well as all of the galaxy-averaged properties.

Our primary conclusions are summarized below.

1. The galaxy reveals significant variations among the physical properties on the spatial scales of individual star clusters. Notably, the compact, small (<100 pc) LyC-leaking region likely harboring a young star cluster exhibits the most extreme physical properties: a very blue UV-continuum slope ($\beta = -2.9 \pm 0.1$), high ionization state ([O III]/[O II] $= 11 \pm 3$ and [O III]/H$\beta = 6.8 \pm 0.4$), strong oxygen emission (EW [O III] $= 1095 \pm 40$ Å), and a high Lyα escape fraction ($f_{\rm esc}$(Lyα)$= 0.3 \pm 0.03$; Figures 2 and 3). Such extreme properties are not found in any nonleaking regions of the galaxy (Section 4.1).
2. The leaking region's blue $\beta \simeq -2.9$ comparison with the starburst population models indicates that its UV emission consists of nearly "pure" stellar light with minimal contamination from surrounding nebular continuum emission and dust extinction (Figure 5). This suggests a direct escape of LyC photons from the ionizing star cluster through an ionized, low N(H I) opening channel(s) (Section 4.2).
3. The leaking region shows higher $f_{\rm esc}$(Lyα) and EW(Lyα) compared to the nonleaking regions (that is, $f_{\rm esc}$(Lyα) of ≈0.3 versus 0.13; EW(Lyα) of ≈43 Å versus 13 Å as in Figure 3 and Table 2). This suggests a similar escape process of LyC and Lyα photons such as preferred low N (H I) channels on subgalactic scales, although the detailed escape pathways can differ from each other due to the larger interaction cross section of Lyα with neutral hydrogen (e.g., Neufeld 1991; Verhamme et al. 2015; Section 4.3).
4. Combined with the different lensing magnification factor and a slightly different viewing angle among the lensed images of the leaking region, the variations found among the physical properties of the lensed leaking region (i.e., the scattered distribution of the black data points in Figures 2 and 3) clearly suggest that the structure of the LyC-leaking region and the associated LyC escape process are highly anisotropic depending on a specific line of sight (Section 4.4). This means that we are viewing the galaxy from a very privileged vantage point through a pencil-beam opening angle. If we had viewed it from most other angles, we may not have seen ionizing escape (Figure 6). Such anisotropic LyC escape from a small, dense star cluster in the Sunburst Arc is only identifiable due to the high magnification from strong lensing, which provides a zoomed-in view of the narrow LyC escape channel. With the presently available observational facilities, spatially resolved studies of LyC leakage are only possible with distant, strongly lensed systems.
5. The integrated galaxy properties are not as extreme as those of the leaking region (i.e., the blue diamonds in Figures 2 and 3), which show $\beta \simeq -2.2$, [O III]/[O II] $\simeq 4$, [O III]/H$\beta \simeq 5$, EW [O III] $\simeq 500$ Å, and $f_{\rm esc}$(Lyα) $\simeq 0.13$. The galaxy properties are rather consistent with those typical of Lyman-break galaxies at similar redshifts (e.g., Hathi et al. 2008) and of local green pea galaxies (e.g., Henry et al. 2015; Izotov et al. 2016b; Yang et al. 2017; Izotov et al. 2021; Flury et al. 2022a; Chisholm et al. 2022). However, the Sunburst Arc is a clear example of a localized, anisotropic process of LyC escape driven by a compact starburst region harboring young star cluster(s), rather than the entire

galaxy contributing to LyC escape. This implies that the true volume-averaged escape fraction of ionizing radiation estimated for individual galaxies may often be subject to large systematic uncertainties due to random line-of-sight effects. It is possible—even likely—that unlensed star-forming galaxies like the Sunburst Arc would have integrated properties that are not indicative of LyC escape but could, in fact, be releasing significant ionizing radiation into the IGM (Section 4.5). These line-of-sight variations are also a natural explanation for the significant scatters between the galaxy properties and LyC escape fraction in the LyC leakers (e.g., Flury et al. 2022b; Izotov et al. 2022; Saxena et al. 2022).

To summarize, our results isolate the physical conditions for LyC escape on very small, subgalactic scales and suggest an anisotropic LyC escape process driven by a compact young star cluster in galaxies. If the Sunburst Arc is representative of how LyC escapes typical star-forming galaxies, then strong lensing is an essential tool for revealing how these galaxies contribute LyC photons to reionization by isolating the physical conditions of a specific LyC-leaking region with boosted spatial magnification. Importantly, our results call for a more sophisticated reionization modeling that accounts for such a directional (anisotropic) LyC escape mode of galaxies.

Going forward, the upcoming JWST IFU study of the Sunburst Arc (GO: 2555; PI: T. Rivera-Thorsen) will further characterize the ISM and the stellar properties of the leaking region by measuring key quantities such as the gas kinematics and dust geometry on spatially resolved scales.

Acknowledgments

We thank the referee for constructive comments that improved the quality of the manuscript. The data presented in this paper were obtained from the Mikulski Archive for Space Telescopes (MAST) at the Space Telescope Science Institute. The specific observations analyzed can be accessed in MAST:10.17909/5bmh-yx42. Support for HST-GO-15101, HST-GO-15418, HST-GO-15377, and HST-GO-15949 was provided by NASA through grants from the Space Telescope Science Institute, which is operated by the Associations of Universities for Research in Astronomy (AURA), Inc., under NASA contract NAS5-26555.

Software: Astrodrizzle (Hack et al. 2012), STScI Development Team (2018), STSYNPHOT/SYNPHOT (Lim 2019).

Appendix A
R.A. and Decl. of the Regions Analyzed

Table 3 lists the R.A. and decl. of the regions analyzed in this study that correspond to the regions shown in Figure 1 and Table 2. The reported values are the centers of individual apertures placed on those regions.

Table 3
List of R.A. and Decl. of the Regions Analyzed

Region	ID[a]	R.A. (deg)	Decl. (deg)
LyC-leaking			
	1	237.530833	−78.182511
	2	237.525563	−78.182751
	3	237.524892	−78.182810
	4	237.519113	−78.183177
	5	237.518263	−78.183252
	6	237.517471	−78.183350
	8	237.501517	−78.186255
	9	237.499804	−78.186744
	10	237.498925	−78.187074
	11	237.493867	−78.190767
Nonleaking			
	1	237.528421	−78.182570
	2	237.528054	−78.182593
	3	237.527658	−78.182611
	4	237.527267	−78.182624
	5	237.523850	−78.182896
	6	237.523546	−78.182930
	7	237.523188	−78.182935
	8	237.520983	−78.183027
	9	237.520621	−78.183065
	10	237.520146	−78.183091
	11	237.529838	−78.182522
	12	237.529383	−78.182528
	13	237.526692	−78.182648
	14	237.526317	−78.182676
	15	237.522508	−78.182943
	16	237.522054	−78.182955
	17	237.521646	−78.182976
	18	237.508696	−78.184758
	19	237.508238	−78.184844
	20	237.50750	−78.184965
	21	237.506454	−78.185157
	22	237.504383	−78.185599
	23	237.502675	−78.186040
	24	237.502267	−78.186133

Note.
[a] ID corresponds to that of Table 2.

Appendix B
Continuum SEDs for Emission Line Measurements

Figure 7 shows the photometry-based SED fits and the associated narrowband filters of the Sunburst Arc we analyzed for continuum subtraction off the emission lines (Section 2.5).

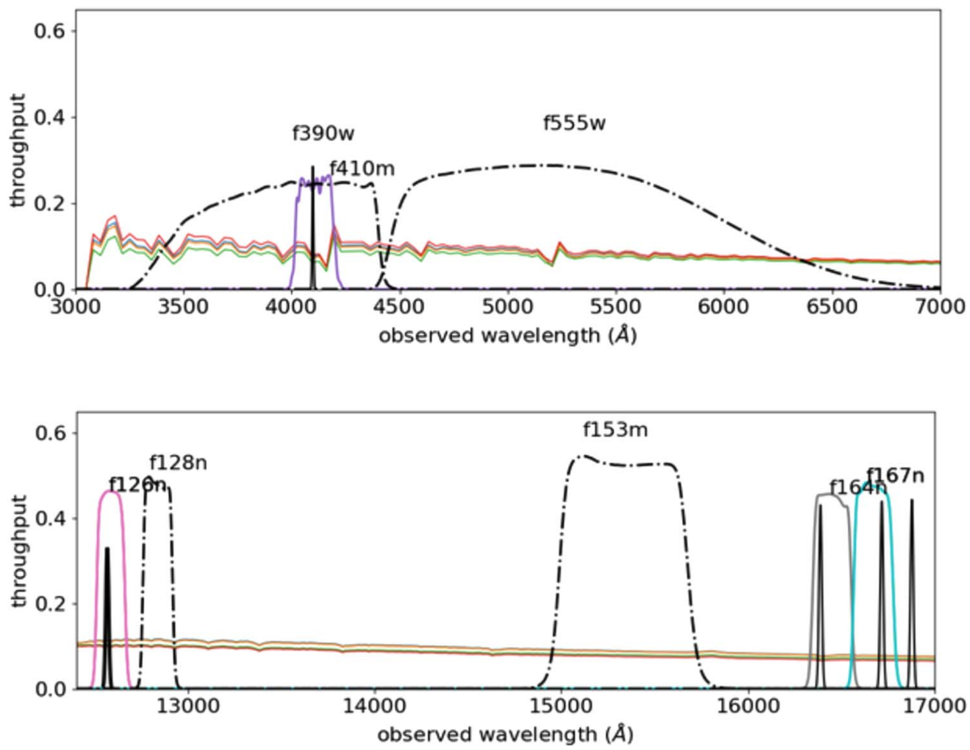

Figure 7. The HST filters and photometric SED fits to subtract off the underlying continuum flux from the narrowband emission lines (Section 2.5). On-band filters are shown with solid curves; off-band continuum filters are plotted as dotted–dashed curves. The *y*-axis is the filter throughput. The best-fit spectra used to determine the continuum fits are overplotted as solid lines, with arbitrary scaling (different in each plot, so as not to obscure the filter curves) in f_λ (units of erg s^{-1} cm^{-2} Å^{-1}). Each of the solid lines corresponds to each of the multiple images of the whole galaxy contained in arcs 1 and 2. In the top panel, the emission line Lyα is overplotted with arbitrary flux. In the bottom panel, the following emission lines are overplotted with arbitrary flux: the [O II] doublet, which falls in the F126N filter; Hβ, which falls in the F164N filter, [O III] λ4959, which falls in the F1647 filter; and [O III] λ5007, which falls just outside the F167N filter.

ORCID iDs

Keunho J. Kim https://orcid.org/0000-0001-6505-0293
Matthew B. Bayliss https://orcid.org/0000-0003-1074-4807
Jane R. Rigby https://orcid.org/0000-0002-7627-6551
Michael D. Gladders https://orcid.org/0000-0003-1370-5010
John Chisholm https://orcid.org/0000-0002-0302-2577
Keren Sharon https://orcid.org/0000-0002-7559-0864
Håkon Dahle https://orcid.org/0000-0003-2200-5606
T. Emil Rivera-Thorsen https://orcid.org/0000-0002-9204-3256
Michael K. Florian https://orcid.org/0000-0001-5097-6755
Gourav Khullar https://orcid.org/0000-0002-3475-7648
Guillaume Mahler https://orcid.org/0000-0003-3266-2001
Ramesh Mainali https://orcid.org/0000-0003-0094-6827
Kate A. Napier https://orcid.org/0000-0003-4470-1696
Alexander Navarre https://orcid.org/0000-0001-7548-0473
M. Riley Owens https://orcid.org/0000-0002-2862-307X
Joshua Roberson https://orcid.org/0000-0002-0975-623X

References

Behrens, C., Dijkstra, M., & Niemeyer, J. C. 2014, A&A, 563, A77
Bergvall, N., & Olofsson, K. 1986, A&AS, 64, 469
Bergvall, N., Zackrisson, E., Andersson, B.-G., et al. 2006, A&A, 448, 513
Bhatawdekar, R., & Conselice, C. J. 2021, ApJ, 909, 144
Borthakur, S., Heckman, T. M., Leitherer, C., et al. 2014, Sci, 346, 216
Bouwens, R. J., Illingworth, G. D., Oesch, P. A., et al. 2010, ApJL, 708, L69
Calzetti, D., Armus, L., Bohlin, R. C., et al. 2000, ApJ, 533, 682
Calzetti, D., Kinney, A. L., & Storchi-Bergmann, T. 1994, ApJ, 429, 582
Cardelli, J. A., Clayton, G. C., & Mathis, J. S. 1989, ApJ, 345, 245
Chisholm, J., Gazagnes, S., Schaerer, D., et al. 2018, A&A, 616, A30
Chisholm, J., Rigby, J. R., Bayliss, M., et al. 2019, ApJ, 882, 182
Chisholm, J., Saldana-Lopez, A., Flury, S., et al. 2022, MNRAS, 517, 5104
Dahle, H., Aghanim, N., Guennou, L., et al. 2016, A&A, 590, L4
Diego, J. M., Pascale, M., Kavanagh, B. J., et al. 2022, A&A, 665, A134
Dijkstra, M. 2019, Saas-Fee Advanced Course, 46, 1
Dopita, M. A., & Sutherland, R. S. 2003, Astrophysics of the Diffuse Universe, Astronomy and Astrophysics Library (Berlin: Springer)
Dunlop, J. S., McLure, R. J., Robertson, B. E., et al. 2012, MNRAS, 420, 901
Fan, X., Carilli, C. L., & Keating, B. 2006, ARA&A, 44, 415
Finkelstein, S. L., D'Aloisio, A., Paardekooper, J.-P., et al. 2019, ApJ, 879, 36
Flury, S. R., Jaskot, A. E., Ferguson, H. C., et al. 2022a, ApJ, 930, 126
Flury, S. R., Jaskot, A. E., Ferguson, H. C., et al. 2022b, ApJS, 260, 1
Gazagnes, S., Chisholm, J., Schaerer, D., et al. 2020, A&A, 639, A85
Gronke, M., Dijkstra, M., McCourt, M., et al. 2016, ApJL, 833, L26
Hack, W. J., Dencheva, N., Fruchter, A. S., et al. 2012, AAS Meeting 220, 135.15
Hathi, N. P., Malhotra, S., & Rhoads, J. E. 2008, ApJ, 673, 686
Henry, A., Scarlata, C., Martin, C. L., et al. 2015, ApJ, 809, 19
Indebetouw, R., de Messières, G. E., Madden, S., et al. 2009, ApJ, 694, 84
Izotov, Y. I., Chisholm, J., Worseck, G., et al. 2022, MNRAS, 515, 2864
Izotov, Y. I., Orlitová, I., Schaerer, D., et al. 2016a, Natur, 529, 178
Izotov, Y. I., Schaerer, D., Thuan, T. X., et al. 2016b, MNRAS, 461, 3683
Izotov, Y. I., Schaerer, D., Worseck, G., et al. 2018a, MNRAS, 474, 4514
Izotov, Y. I., Worseck, G., Schaerer, D., et al. 2018b, MNRAS, 478, 4851
Izotov, Y. I., Worseck, G., Schaerer, D., et al. 2021, MNRAS, 503, 1734
James, B. L., Auger, M., Aloisi, A., et al. 2016, ApJ, 816, 40
Ji, Z., Giavalisco, M., Vanzella, E., et al. 2020, ApJ, 888, 109
Keenan, R. P., Oey, M. S., Jaskot, A. E., et al. 2017, ApJ, 848, 12
Kewley, L. J., & Dopita, M. A. 2002, ApJS, 142, 35
Kewley, L. J., Nicholls, D. C., & Sutherland, R. S. 2019, ARA&A, 57, 511
Kim, K., Malhotra, S., Rhoads, J. E., et al. 2020, ApJ, 893, 134
Kim, K. J., Malhotra, S., Rhoads, J. E., et al. 2021, ApJ, 914, 2
Kimm, T., Bieri, R., Geen, S., et al. 2022, ApJS, 259, 21
Leitet, E., Bergvall, N., Hayes, M., et al. 2013, A&A, 553, A106
Leitet, E., Bergvall, N., Piskunov, N., et al. 2011, A&A, 532, A107

Leitherer, C., Byler, N., Lee, J. C., et al. 2018, ApJ, 865, 55
Leitherer, C., Hernandez, S., Lee, J. C., et al. 2016, ApJ, 823, 64
Leitherer, C., Schaerer, D., Goldader, J. D., et al. 1999, ApJS, 123, 3
Lim, P. L. 2019, synphot v1.0.1, Zenodo, doi:10.5281/zenodo.3971036
Lopez, S., Tejos, N., Barrientos, L. F., et al. 2020, MNRAS, 491, 4442
Mainali, R., Rigby, J. R., Chisholm, J., et al. 2022, arXiv:2210.11575
Malkan, M. A., & Malkan, B. K. 2021, ApJ, 909, 92
Marques-Chaves, R., Schaerer, D., Álvarez-Márquez, J., et al. 2022, MNRAS, 517, 2972
Meurer, G. R., Heckman, T. M., & Calzetti, D. 1999, ApJ, 521, 64
Meštrić, U., Vanzella, E., Upadhyaya, A., et al. 2023, A&A, 673, A50
Micheva, G., Christian Herenz, E., Roth, M. M., et al. 2019, A&A, 623, A145
Micheva, G., Oey, M. S., Jaskot, A. E., et al. 2017, ApJ, 845, 165
Mollá, M., García-Vargas, M. L., & Bressan, A. 2009, MNRAS, 398, 451
Mostardi, R. E., Shapley, A. E., Steidel, C. C., et al. 2015, ApJ, 810, 107
Naidu, R. P., Tacchella, S., Mason, C. A., et al. 2020, ApJ, 892, 109
Nakajima, K., & Ouchi, M. 2014, MNRAS, 442, 900
Nakajima, K., Ouchi, M., Xu, Y., et al. 2022, ApJS, 262, 3
Neufeld, D. A. 1991, ApJL, 370, L85
Östlin, G., Rivera-Thorsen, T. E., Menacho, V., et al. 2021, ApJ, 912, 155
Pascale, M., Dai, L., McKee, C. F., et al. 2023, arXiv:2301.10790
Ramambason, L., Schaerer, D., Stasińska, G., et al. 2020, A&A, 644, A21
Reddy, N. A., Oesch, P. A., Bouwens, R. J., et al. 2018, ApJ, 853, 56
Reddy, N. A., Steidel, C. C., Pettini, M., et al. 2016, ApJ, 828, 107
Rivera-Thorsen, T. E., Dahle, H., Chisholm, J., et al. 2019, Sci, 366, 738
Rivera-Thorsen, T. E., Dahle, H., Gronke, M., et al. 2017, A&A, 608, L4
Rivera-Thorsen, T. E., Hayes, M., Östlin, G., et al. 2015, ApJ, 805, 14
Robertson, B. E., Ellis, R. S., Furlanetto, S. R., et al. 2015, ApJL, 802, L19
Rutkowski, M. J., Scarlata, C., Haardt, F., et al. 2016, ApJ, 819, 81
Rutkowski, M. J., Scarlata, C., Henry, A., et al. 2017, ApJL, 841, L27
Saldana-Lopez, A., Schaerer, D., Chisholm, J., et al. 2022, A&A, 663, A59
Saxena, A., Pentericci, L., Ellis, R. S., et al. 2022, MNRAS, 511, 120
Schaerer, D. 2003, A&A, 397, 527
Seive, T., Chisholm, J., Leclercq, F., et al. 2022, MNRAS, 515, 5556
Shapley, A. E., Steidel, C. C., Strom, A. L., et al. 2016, ApJL, 826, L24
Sharon, K., Mahler, G., Rivera-Thorsen, T. E., et al. 2022, arXiv:2209.03417
Simcoe, R. A., Burgasser, A. J., Schechter, P. L., et al. 2013, PASP, 125, 270
Storey, P. J., & Zeippen, C. J. 2000, MNRAS, 312, 813
STScI Development Team 2018, synphot: Synthetic photometry using Astropy, Astrophysics Source Code Library, ascl:1811.001
Topping, M. W., Stark, D. P., Endsley, R., et al. 2022, arXiv:2208.01610
Vanzella, E., Castellano, M., Bergamini, P., et al. 2022, A&A, 659, A2
Vanzella, E., de Barros, S., Vasei, K., et al. 2016, ApJ, 825, 41
Vanzella, E., Nonino, M., Cupani, G., et al. 2018, MNRAS, 476, L15
Verhamme, A., Orlitová, I., Schaerer, D., et al. 2015, A&A, 578, A7
Wang, B., Heckman, T. M., Leitherer, C., et al. 2019, ApJ, 885, 57
Wofford, A., Leitherer, C., & Salzer, J. 2013, ApJ, 765, 118
Yang, H., Malhotra, S., Gronke, M., et al. 2017, ApJ, 844, 171
Yung, L. Y. A., Somerville, R. S., Finkelstein, S. L., et al. 2020, MNRAS, 496, 4574
Zackrisson, E., Inoue, A. K., & Jensen, H. 2013, ApJ, 777, 39